



Title	Radiolysis-Induced Crystallization of Sodium Chloride in Acetone by Electron Beam Irradiation
Author(s)	Yamazaki, Tomoya; Kimura, Yuki
Citation	Microscopy and microanalysis, 27(3), 459-465 <a href="https://doi.org/10.1017/S1431927621000179">https://doi.org/10.1017/S1431927621000179</a>
Issue Date	2021-05-21
Doc URL	<a href="http://hdl.handle.net/2115/83321">http://hdl.handle.net/2115/83321</a>
Rights	This article has been published in a revised form in Microscopy and Microanalysis <a href="https://doi.org/10.1017/S1431927621000179">https://doi.org/10.1017/S1431927621000179</a> . This version is published under a Creative Commons CC-BY-NC-ND. No commercial re-distribution or re-use allowed. Derivative works cannot be distributed. © The Author(s), 2021. Published by Cambridge University Press on behalf of the Microscopy Society of America .
Rights(URL)	<a href="http://creativecommons.org/licenses/by-nc-nd/4.0/">http://creativecommons.org/licenses/by-nc-nd/4.0/</a>
Type	article (author version)
File Information	Microscopy and microanalysis27(3)_459-465.pdf



[Instructions for use](#)

Radiolysis-Induced Crystallization of Sodium Chloride in Acetone by Electron Beam

Irradiation

(Running title: Radiolysis-Induced Crystallization of Salt)

Tomoya Yamazaki and Yuki Kimura\*

Institute of Low Temperature Science, Hokkaido University, Kita-19, Nishi-8, Kita-ku,  
Sapporo, 060-0819, Japan.

\*Corresponding author: Yuki Kimura (E-mail: ykimura@lowtem.hokudai.ac.jp), TEL/FAX:  
+81-11-706-7666/+81-11-706-7666.

**Abstract:**

In situ liquid cell transmission electron microscopy (LC-TEM) is an innovative method for studying the processes involved in the formation of crystals in liquids. However, it is difficult to capture early stages of crystallization because of the small field of view and the unfavorable changes in sample composition resulting from electron-beam radiolysis. Nevertheless, if the radiolysis required to induce the crystallization of a sample could be controlled in LC-TEM, this would be advantageous for observing the crystallization process. Here we examined this possibility using a mixture of sodium chlorate ( $\text{NaClO}_3$ ) and acetone by LC-TEM. The electron beam induced the formation of dendritic crystals in a saturated acetone solution of  $\text{NaClO}_3$ ; moreover, these crystals consisted of sodium chloride ( $\text{NaCl}$ ), rather than  $\text{NaClO}_3$ , suggesting that chloride ions ( $\text{Cl}^-$ ), which were not present in the initial solution, were generated by radiolysis of chlorate ions ( $\text{ClO}_3^-$ ). As a result, the solution then supersaturated with  $\text{NaCl}$  because its solubility in acetone is much lower than that of  $\text{NaClO}_3$ . The combination of radiolysis and a solvent in which a solute is much less soluble is potentially useful for establishing crystallization conditions for materials that are difficult to crystallize directly in LC-TEM experiments. (199/200 words)

**Key words:** liquid cell transmission electron microscopy, in situ observation, crystallization, radiolysis, solubility, acetone, sodium chloride, sodium chlorate

## **Introduction**

Liquid cell transmission electron microscopy (LC-TEM) is widely used for observing a variety of nanoscale objects and their dynamic behaviors in liquids (de Jonge & Ross, 2011; Ross, 2015). The spatial and temporal resolutions achievable by LC-TEM (de Jonge et al., 2019) suggest that it should be a promising method for observing the early stages of crystallization processes, including the nucleation of crystals (De Yoreo & Sommerdijk, 2016) and, indeed, this method has been employed to observe nucleation processes of such materials as metal nanocrystals (Woehl et al., 2012; Loh et al., 2017), calcium carbonate (Nielsen et al., 2014; Smeets et al., 2015), thenardite (anhydrous sodium sulfate,  $\text{Na}_2\text{SO}_4$ ) (Yuk et al., 2016), metal–organic frameworks (Patterson et al., 2015), and lysozyme protein crystals (Yamazaki et al., 2017).

However, it is difficult to capture the moments of nucleation by LC-TEM. One difficulty is the small size of the observation area. The field of view depends on the magnification, which must be high for the purpose of nanoscale imaging; consequently, the observation area is small. This causes great difficulties in observing the nucleation of materials, especially those with low nucleation rates, because nucleation is a stochastic process. Furthermore, interactions between the specimen and the electron beam can cause various phenomena to occur during TEM observation. In LC-TEM in particular, radiolysis is important, in that can induce dissociation of chemical species in

a sample solution to produce chemically active species that undergo secondary chemical reactions, changing the composition of the solution (Schneider et al., 2014; Ambrožič et al., 2019). The generation of chemical species by radiolysis can be predicted by calculations using a kinetic model (Schneider et al., 2014; Ambrožič et al., 2019). However, the more types of species there are present in a system, the more difficult it becomes to predict the outcome of a radiolytic process.

One strategy available for capturing nucleation events in such situations is to examine the crystallization of species generated by radiolysis. For example, the formation of metal nanoparticles from aqueous solution during LC-TEM can be triggered by the presence of reducing species such as a hydrated electron ( $e_{aq}^-$ ), which is an electron solvated by water ( $e_{sol}^-$ ), or a hydrogen radical ( $H^\cdot$ ) generated by radiolysis (Woehl et al., 2012; Woehl et al., 2013; Loh et al., 2017). Although it is necessary to optimize the experimental conditions and to avoid deleterious effects on the formation of nanoparticles (e.g., electron dose rate-dependent dissolution or degradation of samples) (Hermannsdörfer et al., 2015; Patterson et al., 2015; Yamazaki et al., 2017), it is possible to design a suitable environment for electron-beam-induced crystallization in the field of view of the microscope.

As an example of controlled nucleation during an LC-TEM experiment, we report that the crystallization of sodium chloride (NaCl), which has not been widely studied in

LC-TEM experiments, can be controlled by the electron beam through the use of a solution of sodium chlorate ( $\text{NaClO}_3$ ) in acetone. These findings might permit the development of a new strategy, not only for the observation of nucleation processes, but also for controlling the composition of solutions through an understanding of the radiolysis processes.

## Materials and Methods

Using a liquid cell consisting of a pair of silicon (Si) chips with an amorphous silicon nitride (a-SiN) membrane as an observation window and an LC-TEM holder (Poseidon, Protochips, Inc., Morrisville, NC) equipped with liquid-injection ports, we began our crystallization experiments by mixing a saturated aqueous solution of  $\text{NaClO}_3$  [ $\text{NaClO}_3(\text{aq})$ ] with acetone. The solubility of  $\text{NaClO}_3$  in acetone is much lower than that in water; consequently, mixing a small amount of  $\text{NaClO}_3(\text{aq})$  with a large quantity of acetone usually results in crystallization of  $\text{NaClO}_3$  (Niinomi et al., 2014). We filled the liquid cell of the TEM holder with  $\text{NaClO}_3(\text{aq})$  and filled the inner tube with acetone (Figure 1). To start the observation, acetone was gently pushed out from the syringe to ensure contact between the two solutions. This procedure caused the two solutions to mix slowly through diffusion. We monitored the mixing and subsequent processes by using a field-emission gun transmission electron microscope (JEM-2100F; JEOL Ltd.,

Tokyo), operated at an acceleration voltage of 200 kV. The TEM images were recorded by using a OneView TEM camera (Gatan, Inc., Pleasanton, CA).

We then performed similar observations by using NaClO<sub>3</sub>-saturated acetone, water, and ethanol solutions prepared by dissolving NaClO<sub>3</sub> powder in these solutions at room temperature. These solutions were injected into the liquid cell at flow rates of 2-4 μL min<sup>-1</sup> and observed by LC-TEM; the observations were recorded by using a Flash Camera (JEOL Ltd., Tokyo). Before the experiments, the electron dose rates (e<sup>-</sup> nm<sup>-2</sup>·s<sup>-1</sup>) corresponded to the observation conditions (beam diameter, magnification, spot size, etc.) were measured by using a blank holder, a Faraday cage (JEOL Ltd., Tokyo), and a Model 6485 Picoammeter (Keithley Instruments. Cleveland, OH). The values for the electron dose rate described in this report are those measured before the beam passed through the specimen. In all the experiments, the liquid thickness could be 0.15–0.6 μm (Holtz et al., 2013), considering the 150 nm-thick spacers (Figure. 1) and the effect of the bulging of the window membranes caused by the pressure difference between the liquid sample and the vacuum of the TEM (Jensen & Mølhave, 2016).

We analyzed the TEM images and selected-area electron-diffraction (SAED) patterns by using *imageJ* (Schneider et al., 2012). We used the powder-diffraction files (PDFs) provided by the International Centre for Diffraction Data (ICDD) as the standard

diffraction data, and we simulated the electron-diffraction patterns by using *ReciPro* software (developed by Dr. Y. Seto).

## Results and Discussion

### Observations of Mixtures of Aqueous Sodium Chlorate and Acetone

Before performing our experiments, we had expected to observe crystallization of NaClO<sub>3</sub>, because its supersaturation should have maximized immediately on mixing the two liquids. However, no crystallization was observed, even after a sufficient period had elapsed after the injection of acetone from the syringe. This was because the crystallization had actually occurred at the point where the two liquids mixed. In fact, when we opened the liquid cell, we found that NaClO<sub>3</sub> crystals had formed as a result of increased local supersaturation at the contact point between the two solutions around the small Si chip (Supplementary Figure S1), a similar result to that observed in antisolvent crystallization experiments (Niinomi et al., 2014). Therefore, in the observed region, the solution was not able to maintain a supersaturated state to permit crystallization of NaClO<sub>3</sub>. However, about ten minutes after mixing of solutions, dendritic crystals suddenly formed when we continued to observe the sample without opening the liquid cell (Figure 2 and Supplementary Video 1). When the viewing region was moved to an area where no crystals had formed, a similar phenomenon occurred once more. These

observations showed an obvious feature: that crystallization occurred only in the area irradiated by the electron beam. Furthermore, when the electron dose rate was increased by focusing the electron beam, crystals immediately nucleated exclusively in the area where the beam was focused (Figure 3A–3C and Supplementary Video 2). In addition, when we irradiated the tip of an existing crystal with the electron beam, only that part grew (Figure 3D–3F and Supplementary Video 3). These observations clearly demonstrated that the crystallization was related to and induced by the presence of the electron beam.

From the SAED patterns of the resulting crystals and crystallographic data (Supplementary Table S1), we were surprised to discover that they in fact consisted of NaCl and not NaClO<sub>3</sub> (Figure 4). Note that the SAED patterns of the crystals were recorded through a large bubble (Grogan et al., 2014) because it was difficult to record them in the solution-filled liquid cell, where the electrons were scattered by the solution. As the initial solution contained only sodium ions (Na<sup>+</sup>), chlorate ions (ClO<sub>3</sub><sup>-</sup>), acetone, and water, chloride ions (Cl<sup>-</sup>) must have been generated for NaCl to have formed.

## **Observation of a Saturated Acetone Solution of Sodium Chlorate and the Crystal Growth of Dendritic Crystals of Sodium Chloride**

The sample solution in which the NaCl crystals formed probably consisted of a mixture of acetone and NaClO<sub>3</sub>(aq). To confirm the solution conditions, we prepared a saturated acetone solution of NaClO<sub>3</sub> and observed it flowing into the liquid cell. In this procedure, we also found that NaCl crystals formed in the region irradiated by the electron beam (Figure 5 and Supplementary Table S1). To determine the dependence of the crystal growth on the electron dose rate, we measured the maximum growth rates of dendritic NaCl crystals (Supplementary Figure S2) at three different electron dose rates (Figure 6). Note that we used the maximum growth rate to represent the growth rate at a given electron dose rate because the growth rate changed with time during the measurement (Supplementary Figure S2). The generation of Cl<sup>-</sup> is due to a radiolysis effect, which we will discuss later, and the concentration of Cl<sup>-</sup> reached equilibrium within 10<sup>-3</sup> s from the start of irradiation (Schneider et al., 2014). Under these circumstances, the concentration is assumed to be constant before nucleation and then to start to decrease after nucleation, especially around the crystal, so that a concentration gradient, called the diffusion layer, forms around the crystal. The growth rate decreased after about 20 s, which might correspond to the time needed to create the diffusion layer; this is quite slow compared with the time required for the formation of an equilibrium concentration of Cl<sup>-</sup> by radiolysis. It is therefore reasonable to use the maximum growth rate to represent the growth rate at a given electron dose rate. The growth rates clearly increased

with increasing electron dose rate in this set of experiments (Figure 6A). This showed that the driving force for the growth of NaCl crystal was markedly dependent on the electron dose rate in the region  $39\text{--}157 \text{ e}^- \text{ nm}^{-2} \text{ s}^{-1}$ . An interesting point of this change in growth rate is that an extrapolation of the line of the growth rate of the stem to the origin shows that the growth rate was not below zero for an electron dose rate of zero (Figure 6A). The growth rate ( $R$ ) can be expressed as  $R = \beta\mathcal{Q}(C - C_e)$  where  $\beta$  is a temperature-dependent kinetic coefficient,  $\mathcal{Q}$  is the volume of a growth unit in a crystal,  $C$  is the concentration, and  $C_e$  is the equilibrium concentration (Chernov, 1984). According to this equation, the relationship between the growth rate and the driving force ( $C - C_e$ ) is linear at a constant temperature (there was no significant change in temperature during the LC-TEM experiments). In addition, under equilibrium conditions ( $C - C_e = 0$ ), the growth rate should be zero. As this feature does not appear in Fig. 6A, the relationship between the electron dose rate and driving force is not a simple linear relationship. An interesting tendency can be seen if the growth rate is plotted as a function of the square root of the electron dose rate (Fig. 6B), and this appears to correspond to the equation for the growth rate given above. Further precise analysis is required to understand the relationship between the electron dose rate and the driving force for crystal growth.

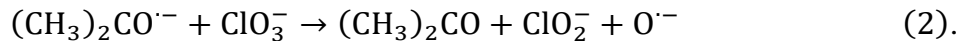
## Electron-Beam-Induced Crystallization Processes

Here, we discuss the crystallization processes in our experiments. For radiolysis in LC-TEM of dilute solutions [in principle, less than 0.1 M (Spothem-Maurizot et al., 2008)], primary radiolysis products are produced mainly from the solvent and are homogeneously distributed in the irradiated area at  $10^{-7}$  s after starting electron beam irradiation (Spothem-Maurizot et al., 2008). These primary products, especially highly reactive species such as solvated electrons and radicals, then react with solutes to produce a variety of chemical species (Schneider et al., 2014; Ambrožič et al., 2019). Our results suggest that the reduction of  $\text{ClO}_3^-$  is a plausible mechanism for the production of  $\text{Cl}^-$ ; therefore, a reducing species for  $\text{ClO}_3^-$  must be generated during primary radiolysis processes. In the radiolysis of water,  $e_{aq}^-$  and  $\text{H}^\bullet$  serve as reducing species with reduction potentials ( $E^\circ$ ) of  $-2.9$  and  $-2.3$  [V], respectively (Woehl & Abellan, 2017). In the case of radiolysis of an acetone–water mixture, it is possible that both these species might be produced. However, acetone is known to act as a scavenger for  $e_{sol}^-$  with production of an acetone radical anion by the following reaction

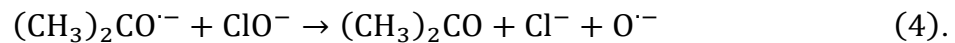
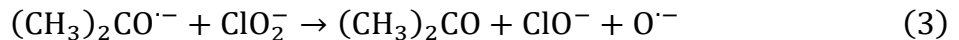


with a rate constant  $k_1 = 7.7 \times 10^9 [\text{M}^{-1} \text{s}^{-1}]$  (Chaudhri & Asmus, 1972; Lai & Freeman, 1990). This acetone radical anion can also be produced directly by electron-beam irradiation as a primary species (Robinson & Rodgers, 1973), and it might serve as a reducing species, albeit

one weaker than  $e_{aq}^-$ , as its reduction potential  $E^\circ[(\text{CH}_3)_2\text{CO}/(\text{CH}_3)_2\text{CO}^-] = -2.1 \text{ [V]}$  (Schwarz & Dodson, 1989). Because the reduction potential of  $\text{ClO}_3^-$  in water  $E^\circ(\text{ClO}_3^-/\text{ClO}_2^-) = 0.33 \text{ [V]}$  (Vanýsek, 2008), it is possible that the acetone radical anion can reduce  $\text{ClO}_3^-$  to  $\text{ClO}_2^-$  by the following reaction



Similarly, the acetone radical anion can reduce  $\text{ClO}_3^-$  to  $\text{Cl}^-$  in a stepwise process following reaction (2):



The reductions of  $\text{ClO}_3^-$ ,  $\text{ClO}_2^-$ , and  $\text{ClO}^-$  by  $e_{aq}^-$  proceed with rate constants of  $< 10^6$ ,  $(4.5 \pm 0.5) \times 10^{10}$ , and  $(5.3 \pm 1.0) \times 10^{10} \text{ [M}^{-1} \text{ s}^{-1}\text{]}$ , respectively (Buxton & Subhani, 1972). Therefore, the reduction of  $\text{ClO}_3^-$  to  $\text{ClO}_2^-$  is the rate-limiting reaction in this stepwise reduction of  $\text{ClO}_3^-$  to  $\text{Cl}^-$ .

In the case of  $\text{H}^\bullet$  as a reducing agent,  $\text{ClO}_3^-$  can be reduced by the following series of reactions:



with reference to the proposed reaction for the reduction of  $\text{ClO}_2^-$  and  $\text{ClO}^-$  (Buxton & Subhani, 1972).

In the case of acetone solutions, a variety of products, including molecular ions (anions and cations) and excited molecules, are generated as reactive species by the primary processes (Rodgers, 1971; Robinson & Rodgers, 1973; Akhtar et al., 1975). In this case, the acetone radical anion can operate as the reducing agent described above.

A certain time after initiation of electron beam irradiation, the local concentrations of not only  $\text{Cl}^-$ , but all other chemical species generated by chemical reactions in the irradiated region become practically constant (Schneider et al., 2014). These concentrations are determined by a balance between destruction and production of the relevant species through chemical reactions and diffusion (Schneider et al., 2014).

For NaCl crystals to form in acetone under these conditions, the value of its saturation index  $SI$  [ $SI = a_{(\text{Na}^+)} \cdot a_{(\text{Cl}^-)} / K_{\text{sp}(\text{NaCl})}$ , where  $a$  is the activity and  $K_{\text{sp}}$  is the solubility product] should exceed 1. The activity can be expressed as  $a = \gamma m$  where  $\gamma$  is activity coefficient and  $m$  is the concentration [here, we use molality ( $\text{mol kg}^{-1}$ )]. According to the Debye–Hückel limiting law, the activity coefficient  $\gamma$  is close to 1 when the ionic strength of the solution is close to 0. In the LC-TEM experiments, it is likely that in the solution a variety of ions are generated and destroyed simultaneously by the radiolysis process; it is therefore difficult to calculate the exact value of the ionic strength by using the concentrations of all the ions. For this reason we attempted to estimate the concentration of generated  $\text{Cl}^-$ , at least as a guide, by calculating it from the solubility

of NaCl in acetone (Burgess, 1978) (Table 1). By assuming that the activity coefficient is 1 and ignoring side reactions such as ion association, we obtained a value of  $K_{\text{sp}(\text{NaCl})}$   $\approx 5.2 \times 10^{-11} \text{ mol}^2 \text{ kg}^{-2}$ . Before electron beam irradiation of the sample, the concentrations  $[\text{Na}^+]$  and  $[\text{Cl}^-]$  are  $8.9 \times 10^{-3}$  (Miyamoto & Salomon, 1987) (Table 1) and  $0 \text{ mol kg}^{-1}$ , respectively. After electron beam irradiation,  $[\text{Cl}^-]$  starts to increase, and NaCl crystallizes when  $SI \geq 1$ . For this condition to occur,  $[\text{Cl}^-]$  must exceed  $5.8 \times 10^{-9} \text{ mol kg}^{-1}$ .

To verify this, the total quantity of  $\text{Cl}^-$  generated in the irradiated region was calculated by using the calculated  $[\text{Cl}^-]$ , the beam diameter ( $\sim 8.5 \mu\text{m}$ ), the thickness of liquid layer taking bulding into account [ $\sim 0.15\text{--}0.6 \mu\text{m}$  (Holtz et al., 2013)], and the density of acetone ( $\sim 0.784 \text{ g cm}^{-3}$ ) this calculation gave a value of  $(3.9 \text{ to } 15) \times 10^{-23} \text{ mol}$ . This value is quite small, and the corresponding number of ions could only form NaCl crystals with a size of  $1.0\text{--}4.2 \text{ nm}^3$ . This shows that a supersaturated condition for NaCl crystals in acetone could result from the presence of a very small number of ions. In actual experiments, the total number of  $\text{Cl}^-$  ions generated by radiolysis would have been greater, because  $7.4 \times 10^{-15} \text{ mol}$  of  $\text{Cl}^-$  are required to produce an NaCl crystal with a volume of  $0.2 \mu\text{m}^3$ , the volume roughly calculated for the crystal in Fig. 5C, which had an area of  $1.48 \mu\text{m}^2$  and an assumed thickness of  $0.15 \mu\text{m}$ . Therefore, the actual number of  $\text{Cl}^-$  generated by radiolysis is far greater than that calculated from the solubility.

## **Crystal shape**

Here we describe some interesting phenomena observed during our experiments. The shapes of the crystals that formed were mostly dendritic with stems that grew in the  $<100>$  direction, as determined from their SAED patterns (Figures 4 and 5). According to the crystal symmetry, the equilibrium shape of the crystal is a regular octahedron, and the observed dendritic crystals were formed by faster growth of the tips of the octahedron, showing that the ideal number of stems of each dendritic crystal is six. However, the number of the stems of the observed crystals was three to five, suggesting that the growth of some directions is inhibited by the SiN window substrate. If the crystals nucleated in solution homogeneously, crystals with six stems should have been observed. However, we did not observe any such crystals during our experiments, implying that all crystals nucleated on the SiN window heterogeneously.

In addition, the growth shape of the observed crystals was not the same as that observed in aqueous solution. In aqueous solution, the growth shape of a NaCl crystals is generally rectangular and the direction of the growth of dendrites is generally  $<110>$  or  $<111>$  (Goto et al., 2016). It is commonly observed that the growth shape of NaCl crystals is dependent on the solvent (Stoica et al., 2004) and that the shape of NaCl crystals can be changed by the presence of an organic additive in an aqueous solution of NaCl

(Townsend et al., 2018). In our experiments, the dendritic shape of the NaCl crystal was caused by the acetone, possibly due to differences in solvent–surface interactions from those in aqueous solution inducing drastic changes in facial growth rates (Stoica et al., 2004). We also found that the shapes of the growing crystals changed when many crystals nucleated in the same view (Supplementary Figure S3A–B). The crystals that formed in small regions between the dendrites had a rounded shape, suggesting that the supersaturation in these regions was too low to permit the formation of dendrites (Supplementary Figure S3A). In addition, in some sets of experiments using a saturated solution of NaClO<sub>3</sub> in acetone, rounded crystals formed immediately after electron beam irradiation (Supplementary Figure S3B). This was because many crystals formed simultaneously due to the high nucleation rate; this would have resulted in a high rate of consumption of Cl<sup>−</sup> ions, so that the degree of supersaturation in this region was not sufficiently high to permit the formation of dendrites. Thus, the variation in the form of the crystals reflects the conditions under which they were formed. The other possibility for changing the crystal shape is the formation of defects by the electron beam. An electron beam can induce the formation of crystal defects such as point defects or dislocations. Such defects can change the solubility of a crystal and the crystal-growth mode, which can affect the shape of a crystal. Although we have not yet observed the

existence of any such defects, we intend to investigate the effects of the electron dose rate on defect formation in relation to crystal growth.

### **Similar Experiments in Other Solvents**

To explore the possibility of reproducing similar results in other solvents, we prepared saturated solutions of NaClO<sub>3</sub> in water and in ethanol, two solvents in which the solubilities of both NaCl (Burgess, 1978; Pinho & Macedo, 1996) and NaClO<sub>3</sub> (Chen et al., 2002) have been investigated (Table 1), and we performed similar sets of experiments. However, we did not observe any crystals in either case (Supplementary Figure S4). In the case of the saturated aqueous NaClO<sub>3</sub> solution, a large air bubble formed in the liquid cell (Supplementary Figure S4B) and this spread over the entire view making further observation impossible. Possible reasons for the lack of crystal formation include the greater solubilities of NaCl and NaClO<sub>3</sub> in water and in ethanol compared with those in acetone (Table 1) or differences in the radiolysis processes in these solvents compared with that in acetone. The high solubilities of NaCl in water and in ethanol prevent the formation of the supersaturated conditions necessary for crystallization of NaCl, due to insufficient generation of Cl<sup>-</sup> ions. From the viewpoint of radiolysis, the reducing species required for the generation of Cl<sup>-</sup> are produced by radiolysis in either water or ethanol (Spothem-Maurizot et al., 2008). However, in the case of water, the hydroxyl radical oxidizes ClO<sub>3</sub><sup>-</sup> to ClO<sub>4</sub><sup>-</sup>, which has quite low reaction

rates with  $e_{aq}^-$  and H (Kataxis & Allen, 1964). It is therefore possible that the presence of  $\text{ClO}_4^-$  prevents further reactions, resulting in suppression of NaCl crystallization. In the case of ethanol, the rate constant for the reaction of  $e_{sol}^-$  with an ethanol molecule is quite low (Woehl & Abellan, 2017) and  $e_{sol}^-$  can operate as a reducing agent for  $\text{ClO}_3^-$ . In this case, however, the high solubility of NaCl in ethanol prevents the creation of the supersaturated conditions necessary for NaCl crystallization. The establishment of a strategy for creating supersaturated conditions based on radiolysis and solubility would be beneficial for LC-TEM experiments.

## Conclusion

We succeeded in observing the crystallization of NaCl by a combination of electron beam radiolysis and the use of acetone as a solvent with an extremely low solubility for NaCl. This concept involving a combination of radiolysis and a solvent change to control solubility is an option for designing a crystallization method in LC-TEM experiments, and should permit the crystallization of materials that are highly soluble in water and that would otherwise be difficult to crystallize in a liquid cell. The method should also be helpful in achieving an understanding of both positive and negative effects of radiolysis on an observed system, which is a major technical interest in LC-TEM experiments.

## Acknowledgements

We are grateful to Mr. T. Saeki (AMETEK Co., Ltd) for technical assistance with imaging using a CMOS camera (OneView IS, Gatan, Inc.). We would like to thank K. Kitajima (Hokkaido Univ.) for useful discussions. This work was supported by a Grant for Basic Science Research Projects from the Sumitomo Foundation (Grant Number 170738) and by JSPS KAKENHI, grants numbers JP15H05731, JP18J01470, JP18K14134, JP20H00323, and JP20H05657. T.Y. is grateful for a research fellowship from the Japan Society for the Promotion of Science for Young Scientists.

## References

- AKHTAR, S. M. S., WOODS, R. J. & BARDWELL, J. A. E. (1975).  $\gamma$ -Radiolysis of liquid acetone, methyl ethyl ketone and diethyl ketone. *Int. J. Radiat. Phys. Chem.* **7**, 603–610.
- AMBROŽIČ, B., PRAŠNIKAR, A., HODNIK, N., KOSTEVŠEK, N., LIKOZAR, B., ROŽMAN, K. Ž. & ŠTURM, S. (2019). Controlling the radical-induced redox chemistry inside a liquid-cell TEM. *Chem. Sci.* **10**, 8735–8743.
- BURGESS, J. (1978). *Metal Ions in Solution*. Chichester, UK: Ellis Horwood.
- BUXTON, G. V. & SUBHANI, M. S. (1972). Radiation chemistry and photochemistry of oxychlorine ions. Part 2. Photodecomposition of aqueous solutions of hypochlorite ions.

*J. Chem. Soc., Faraday Trans. I* **68**, 958–969.

CHAUDHRI, S. A. & ASMUS, K. D. (1972). Ion yields and ion neutralization processes in pulse-irradiated acetone. *J. Phys. Chem.* **76**, 26–31.

CHEN, W. C., LIU, D. D., MA, W. Y., XIE, A. Y. & FANG, J. (2002). The determination of solute distribution during growth and dissolution of NaClO<sub>3</sub> crystals: The growth of large crystals. *J. Cryst. Growth* **236**, 413–419.

CHERNOV, A. A. (1984). *Modern Crystallography III*. Berlin: Springer.

DE JONGE, N., Houben, L., DUNIN-BORKOWSKI, R. E. & ROSS, F. M. (2019). Resolution and aberration correction in liquid cell transmission electron microscopy. *Nat. Rev. Mater.* **4**, 61–78.

DE JONGE, N. & ROSS, F. M. (2011). Electron microscopy of specimens in liquid. *Nat. Nanotechnol.* **6**, 695–704.

DE YOREO, J. J. & SOMMERDIJK, N. A. J. M. (2016). Investigating materials formation with liquid-phase and cryogenic TEM. *Nat. Rev. Mater.* **1**, 16035.

GOTO, M., OAKI, Y. & IMAI, H. (2016). Dendritic growth of NaCl crystals in a gel matrix: Variation of branching and control of bending. *Cryst. Growth Des.* **16**, 4278–4284.

GROGAN, J. M., SCHNEIDER, N. M., ROSS, F. M. & BAU, H. H. (2014). Bubble and pattern formation in liquid induced by an electron beam. *Nano Lett.* **14**, 359–364.

HERMANNSDÖRFER, J., DE JONGE, N. & VERCH, A. (2015). Electron beam induced chemistry of

- gold nanoparticles in saline solution. *Chem. Commun.* **51**, 16393–16396.
- HOLTZ, M. E., YU, Y. C., GAO, J., ABRUÑA, H. D. & MULLER, D. A. (2013). In situ electron energy-loss spectroscopy in liquids. *Microsc. Microanal.* **19**, 1027–1035.
- JENSEN, E. & MØLHAVE, K. (2016). Encapsulated liquid cells for transmission electron microscopy. In Liquid Cell Electron Microscopy, Ross F. M. (Ed.), pp. 35–55. Cambridge, New York: Cambridge University Press.
- KATAKIS, D. & ALLEN, A. O. (1964). The radiolysis of aqueous perchloric acid solutions. *J. Phys. Chem.* **68**, 3107–3115.
- LAI, C. C. & FREEMAN, G. R. (1990). Solvent effects on the reactivity of solvated electrons with organic solutes in methanol/water and ethanol/water mixed solvents. *J. Phys. Chem.* **94**, 302–308.
- LOH, N. D., SEN, S., BOSMAN, M., TAN, S. F., ZHONG, J., NIJHUIS, C. A., KRÁL, P., MATSUDAIRA, P. & MIRSAIDOV, U. (2017). Multistep nucleation of nanocrystals in aqueous solution. *Nat. Chem.* **9**, 77–82.
- MIYAMOTO, H. & SALOMON, M. (Eds.) (1987). *Alkali Metal Halates, Ammonium Iodate and Iodic Acid, IUPAC Solubility Data Series. Vol. 30.* Oxford, UK: Pergamon.
- NIELSEN, M. H., ALONI, S. & DE YOREO, J. J. (2014). In situ TEM imaging of CaCO<sub>3</sub> nucleation reveals coexistence of direct and indirect pathways. *Science* **345**, 1158–1162.
- NIINOMI, H., HORIO, A., HARADA, S., UJIHARA, T., MIURA, H., KIMURA, Y. & TSUKAMOTO, K.

(2014). Solubility measurement of a metastable achiral crystal of sodium chlorate in solution growth. *J. Cryst. Growth* **394**, 106–111.

PATTERSON, J. P., ABELLAN, P., DENNY, M. S. JR., PARK, C., BROWNING, N. D., COHEN, S. M., EVANS, J. E. & GIANNESCHI, N. C. (2015). Observing the growth of metal–organic frameworks by *in situ* liquid cell transmission electron microscopy. *J. Am. Chem. Soc.* **137**, 7322–7328.

PINHO, S. P. & MACEDO, E. A. (1996). Representation of salt solubility in mixed solvents: A comparison of thermodynamic models. *Fluid Phase Equilib.* **116**, 209–216.

ROBINSON, A. J. & RODGERS, M. A. J. (1973). Primary processes in acetone radiolysis. *J. Chem. Soc., Faraday Trans. 1* **69**, 2036–2045.

RODGERS, M. A. J. (1971). Pulse radiolysis studies of acetone solutions. *Trans. Faraday Soc.* **67**, 1029–1040.

Ross, F. M. (2015). Opportunities and challenges in liquid cell electron microscopy. *Science* **350**, aaa9886.

SCHNEIDER, C. A., RASBAND, W. S. & ELICEIRI, K. W. (2012). NIH Image to ImageJ: 25 years of image analysis. *Nat. Methods* **9**, 671–675.

SCHNEIDER, N. M., NORTON, M. M., MENDEL, B. J., GROGAN, J. M., ROSS, F. M. & BAU, H. H. (2014). Electron–water interactions and implications for liquid cell electron microscopy. *J. Phys. Chem. C* **118**, 22373–22382.

- SCHWARZ, H. A., & DODSON, R. W. (1989). Reduction potentials of  $\text{CO}^{2-}$  and the alcohol radicals. *J. Phys. Chem.* **93**, 409–414.
- SMEETS, P. J. M., CHO, K. R., KEMPEN, R. G. E., SOMMERDIJK, N. A. J. M. & DE YOREO, J. J. (2015). Calcium carbonate nucleation driven by ion binding in a biomimetic matrix revealed by in situ electron microscopy. *Nat. Mater.* **14**, 394–399.
- SPOTHEM-MAURIZOT, M., MOSTAFAVI, M., DOUKI, T., & BELLONI, J. (Eds.) (2008). *Radiation Chemistry: From Basics to Applications in Materials and Life Sciences*. Les Ulis, France: EDP Sciences.
- STOICA, C., VERWER, P., MEEKES, H., VAN HOOF, P. J. C. M., KASPERSEN, F. M. & VLIEG, E. (2004). Understanding the effect of a solvent on the crystal habit. *Cryst. Growth Des.* **4**, 765–768.
- TOWNSEND, E. R., VAN ENCKEVORT, W. J. P., TINNEMANS, P., BLIJLEVENS, M. A. R., MEIJER, J. A. M. & VLIEG, E. (2018). Additive induced formation of ultrathin sodium chloride needle crystals. *Cryst. Growth Des.* **18**, 755–762.
- WOEHL, T. J., EVANS, J. E., ARSLAN, I., RISTENPART, W. D. & BROWNING, N. D. (2012). Direct in situ determination of the mechanisms controlling nanoparticle nucleation and growth. *ACS Nano* **6**, 8599–8610.
- VANÝSEK, P. (2008). Electrochemical Series. In CRC Handbook of Chemistry and Physics, 89<sup>th</sup> edition, Lide, D. R. (ed.), pp. 20–29. Boca Raton, Florida: CRC Press.

- WOEHL, T. J., JUNGJOHANN, K. L., EVANS, J. E., ARSLAN, I., RISTENPART, W. D. & BROWNING, N. D. (2013). Experimental procedures to mitigate electron beam induced artifacts during in situ fluid imaging of nanomaterials. *Ultramicroscopy* **127**, 53–63.
- WOEHL, T. J. & ABELLAN, P. (2017). Defining the radiation chemistry during liquid cell electron microscopy to enable visualization of nanomaterial growth and degradation dynamics. *J. Microsc. (Oxford, U. K.)* **265**, 135–147.
- YAMAZAKI, T., KIMURA, Y., VEKILOV, P. G., FURUKAWA, E., SHIRAI, M., MATSUMOTO, H., VAN DRIESSCHE, A. E. S. & TSUKAMOTO, K. (2017). Two types of amorphous protein particles facilitate crystal nucleation. *Proc. Natl. Acad. Sci. U. S. A.* **114**, 2154–2159.
- YUK, J. M., ZHOU, Q., CHANG, J., ERCIUS, P., ALIVISATOS, A. P. & ZETTL, A. (2016). Real-time observation of water-soluble mineral precipitation in aqueous solution by in situ high-resolution electron microscopy. *ACS Nano* **10**, 88–92.

## Tables

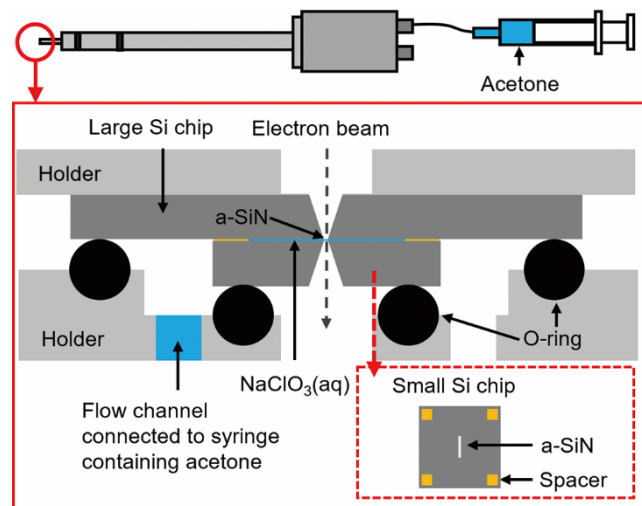
**Table 1.** Solubilities of NaCl and NaClO<sub>3</sub> in various solvents at 25 °C. The values were calculated based on the references. The solubility of NaClO<sub>3</sub> in ethanol was measured by comparing the weights of a certain amount of a saturated ethanol solution of NaClO<sub>3</sub> and its deposit after evaporation.

Solvent	NaCl		References
	g 100g <sup>-1</sup>	mol kg <sup>-1</sup>	
Acetone	$4.2 \times 10^{-5}$	$7.2 \times 10^{-6}$	(Burgess, 1978)
H <sub>2</sub> O	36	6.2	(Burgess, 1978)
Ethanol	$5.5 \times 10^{-2}$	$1.6 \times 10^{-2}$	(Pinho & Macedo, 1996)

Solvent	NaClO <sub>3</sub>		References
	g 100g <sup>-1</sup>	mol kg <sup>-1</sup>	
Acetone	$9.4 \times 10^{-2}$	$8.9 \times 10^{-3}$	(Miyamoto & Salomon, 1987)
H <sub>2</sub> O	98.7	9.3	(Chen et al., 2002)
Ethanol	0.38	$3.6 \times 10^{-2}$	—

## Figures



**Figure 1.** Schematic representations of the TEM holder and a cross-section of the liquid cell.

A syringe containing about 2 mL of acetone was connected to the TEM holder. An enlarged cross-section of the liquid cell at the tip of the TEM holder is shown in the region inside the solid red rectangle. A supersaturated aqueous solution of NaClO<sub>3</sub> [NaClO<sub>3</sub>(aq)] was sandwiched between the large silicon (Si) chip and the small Si chip, a top view of which is shown in the rectangle inside the broken red line. Both Si chips were equipped with amorphous silicon nitride (a-SiN) observation windows. The small Si chip was also equipped with 150 nm-thick gold spacers at its four corners. The acetone was introduced into the liquid cell through the flow channel by pushing the syringe. The liquid cell was made vacuum tight by means of a perfluoroelastomer O-ring, which has good chemical resistance to acetone. The schematics are not drawn to scale.

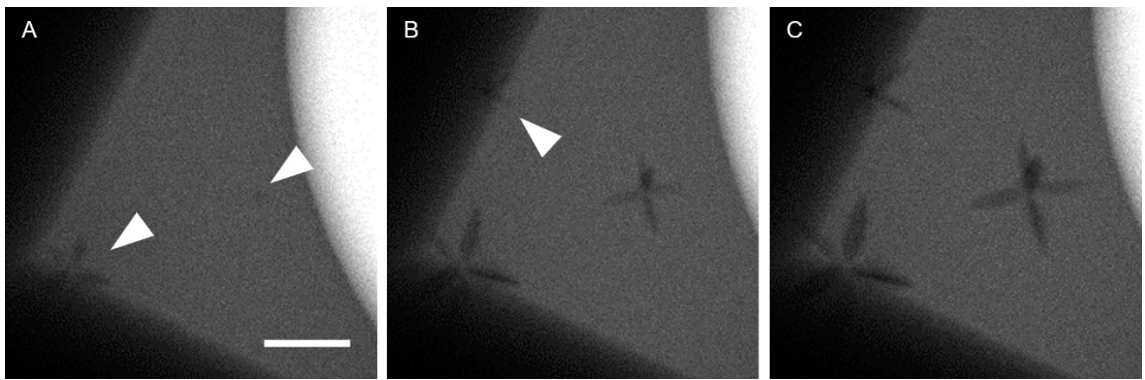


**Figure 2.** A series of bright-field TEM images of the crystallization of a dendrite from an aqueous solution of  $\text{NaClO}_3$  mixing with acetone. This event is the same as that shown in Supplementary Video 1, recorded ten minutes after mixing the solutions. The three images were captured at about 10 (A), 15 (B), and 20 s (C), respectively, after the area had been irradiated by the electron beam. The white arrowheads indicate the positions at which crystallizations occurred. The edge of the a-SiN window is visible in the top and bottom left-hand corners of the image, and a bubble is visible in the top right-hand corner of each image. The electron dose rate was  $37 \text{ e}^- \text{ nm}^{-2} \cdot \text{s}^{-1}$ . The scale bar is  $2 \mu\text{m}$ .

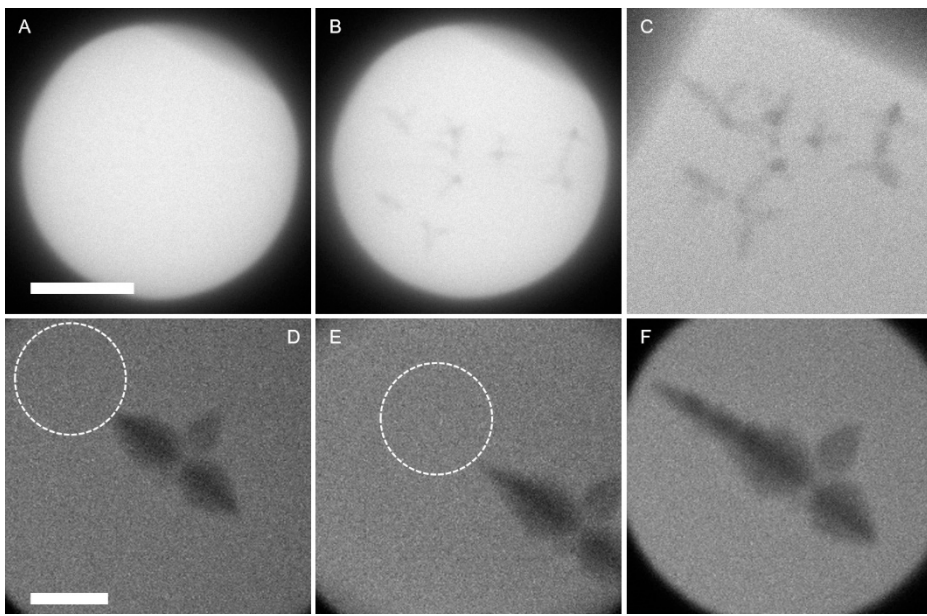


**Figure 3.** Electron-beam-induced crystallization. (A–C) Series of bright-field TEM images of beam-induced nucleation. This event is the same as that shown in Supplementary Video 2. After commencement of irradiation by the electron beam at an electron dose rate of  $120 \text{ e}^- \text{ nm}^{-2} \cdot \text{s}^{-1}$  (A), several dendrites nucleated within 1.4 s (B). No crystals formed outside the area where the electron beam was focused (C). The edge of the a-SiN window is visible in the top left-hand and right-hand corners. The scale bar is 2  $\mu\text{m}$ , and the scale in (B, C) is the same as that in (A). (D–F) Series of bright-field TEM images of beam-induced crystal growth. This event is the same as that shown in Supplementary Video 3. Images E and F were captured 9.1 and 27.3 s, respectively, after Image D. In Images D and E, the electron beam was focused in the area surrounded by the broken line for 5.6 and 11.3 s, respectively. The electron dose rate of the focused beam was  $420 \text{ e}^- \text{ nm}^{-2} \cdot \text{s}^{-1}$ . The top left part of the crystal near the focused electron beam grew faster than the other part of the crystal (F). The scale bar is 2  $\mu\text{m}$ , and the scale in (E, F) is the same as that in (D).

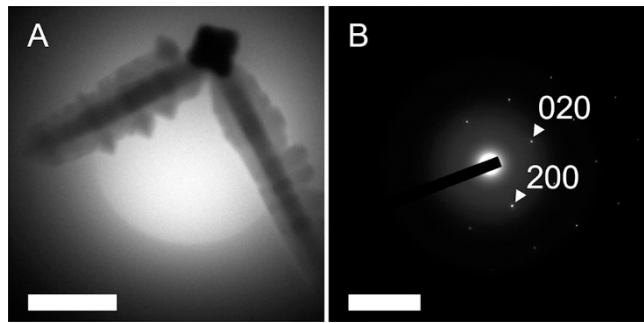


**Figure 4.** Identification of a crystal that formed in a mixed solution of water and acetone. (A) The dendritic crystal and (B) its SAED pattern, corresponding to the [001] SAED pattern of NaCl (ICDD PDF No. 5-628). The measured d-spacings  $d_{hkl}$  are  $d_{200} = 2.94 \text{ \AA}$  and  $d_{020} = 2.93 \text{ \AA}$ . The circular object in (A) is a selected-area diffraction aperture. The scale bars are  $2 \mu\text{m}$  (A) and  $5 \text{ nm}^{-1}$  (B).

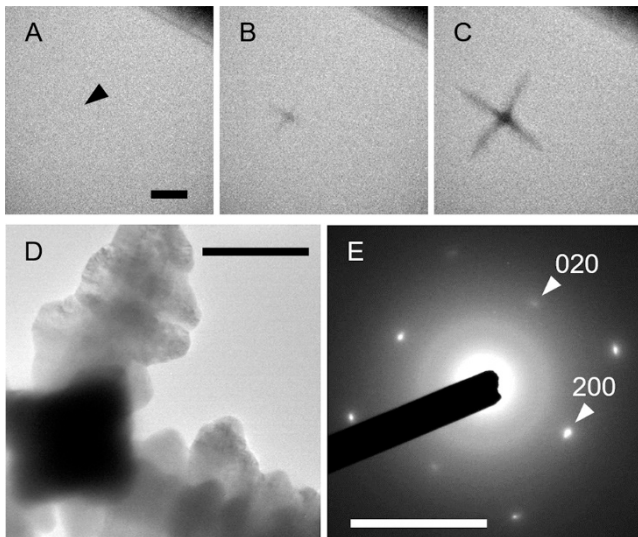


**Figure 5.** Crystallization of dendrites in a saturated acetone solution of  $\text{NaClO}_3$ . (A–C) A series of bright-field TEM images of a crystallizing dendrite. Images were captured within 1 s (A), and at about 5 s (B) and 15 s (C) after the area had been irradiated by the electron beam. The black arrowheads indicate the positions at which nucleation occurred. The edge of the a-SiN window is visible in the top right-hand corner. The electron dose rate was  $78 \text{ e}^- \text{ nm}^{-2} \cdot \text{s}^{-1}$ . The scale bar is 1  $\mu\text{m}$ , and the scale of (B, C) is the same as that of (A). (D–E) Identification of a formed crystal: (D) dendritic crystal (which was different from the crystal in A–C) and (E) its SAED pattern, corresponding to that of NaCl (JCPDS Card No. 5-0628) with a crystallographic orientation of [001]. The measured d-spacings  $d_{hkl}$  are  $d_{200} = 2.81 \text{ \AA}$  and  $d_{020} = 2.84 \text{ \AA}$ . The scale bars are 1  $\mu\text{m}$  (D) and 5  $\text{nm}^{-1}$  (E).

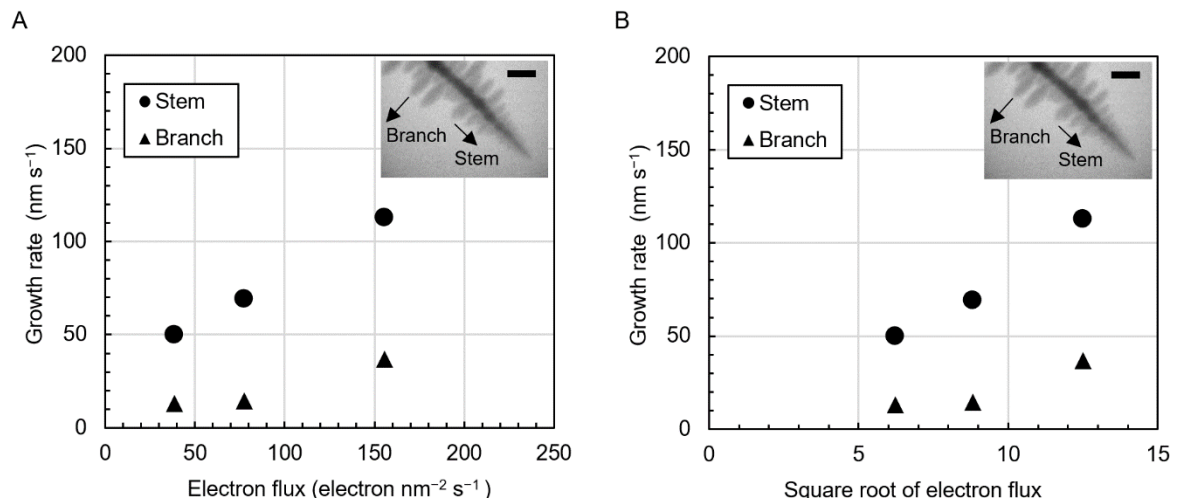


**Figure 6.** Growth rates of dendrites as a function of the electron dose rate (A) or the square root of the electron dose rate (B) under the experimental conditions. The inset shows a typical dendritic crystal and the directions in which the growth rate was measured. The scale bar in inset is 1  $\mu\text{m}$ .

## Supplementary Information

# Radiolysis-Induced Crystallization of Sodium Chloride in Acetone by Electron Beam Irradiation

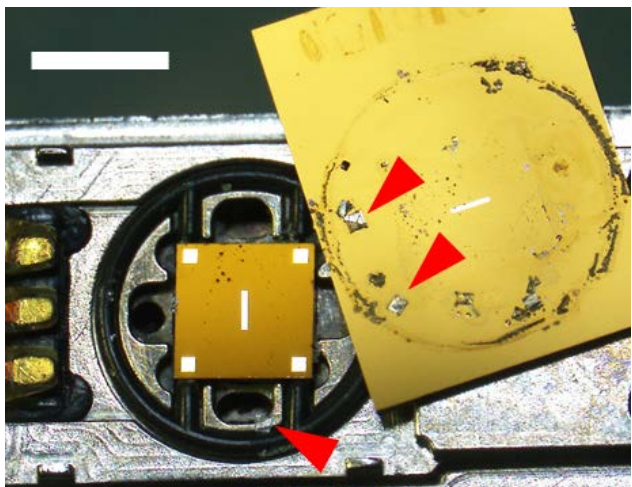
*Tomoya Yamazaki and Yuki Kimura\**

Institute of Low Temperature Science, Hokkaido University.

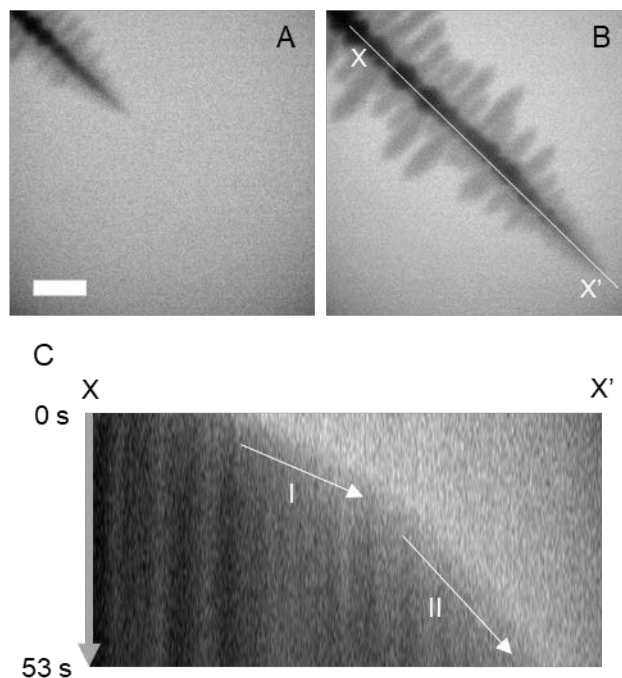
\*Corresponding author: [ykimura@lowtem.hokudai.ac.jp](mailto:ykimura@lowtem.hokudai.ac.jp)

**Supplementary Figures S1–S4**

**Supplementary Videos 1–3**

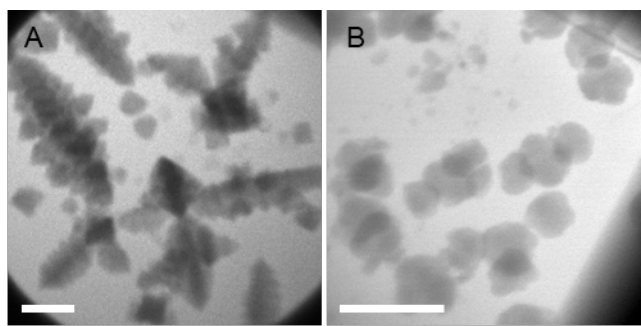


**Supplementary Figure S1.** Crystallization of  $\text{NaClO}_3$  outside the observable view of the liquid cell after mixing of the solutions. The red arrowheads indicate  $\text{NaClO}_3$  crystals. The scale bar (top left-hand corner) is 2 mm.



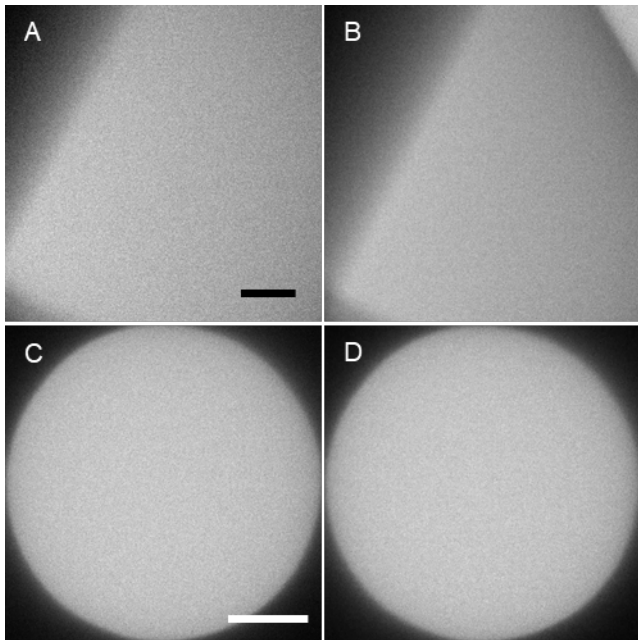
**Supplementary Figure S2.** Measurement of the maximum growth rate of a dendritic crystal.

The crystal was grown during 53 s (A: 0 s, B: 53 s) at an electron flux of 156 electrons  $\text{nm}^{-2} \cdot \text{s}^{-1}$ . The displacement of the tip of the stem is visualized by a time–space plot image (C) along the X–X' line in (B), and the slope in this image corresponds to the growth rate. The time–space plot image shows that the growth rate during first 20 s (white arrow I;  $113 \text{ nm s}^{-1}$ ) was larger than that during the subsequent 33 s (white arrow II;  $63 \text{ nm s}^{-1}$ ). Therefore, the maximum growth rate under these conditions was measured from white arrow I as  $113 \text{ nm s}^{-1}$ . The scale bars are  $1 \mu\text{m}$  (A).



**Supplementary Figure S3.** Various crystals observed in the LC-TEM experiments. (A–B)

Rounded crystals formed during the LC-TEM experiments. These rounded crystals formed between dendritic crystals in the mixture of water and acetone solutions (A). The rounded crystals mainly formed in the acetone solution. The electron dose rates were 18 electrons  $\text{nm}^{-2} \cdot \text{s}^{-1}$  (A) and 200 electrons  $\text{nm}^{-2} \cdot \text{s}^{-1}$  (B). The scale bars are 2  $\mu\text{m}$ .



**Supplementary Figure S4.** Beam effects on saturated aqueous and ethanolic solutions of  $\text{NaClO}_3$ . (A–B) No crystals formed in saturated aqueous  $\text{NaClO}_3$  at an electron dose rate of 35 electrons  $\text{nm}^{-2} \cdot \text{s}^{-1}$  during 120 s. Images were captured at about 40 (A) and 120 s (B) after the area had been irradiated by the electron beam. The scale bar is 1  $\mu\text{m}$ , and the scale of (B) is the same as that of (A). The edge of the a-SiN window is visible in the top and bottom left-hand corners (A and B), and a bubble is visible at the top right-hand corner in (B). (C–D) No crystal was formed in saturated ethanolic  $\text{NaClO}_3$  at an electron dose rate of 2000 electrons  $\text{nm}^{-2} \cdot \text{s}^{-1}$  during 140 s. Images were captured within 1 s (C) and at 140 s (D) after the area had been irradiated by the electron beam. The scale bar is 1  $\mu\text{m}$ , and the scale of (D) is the same as that of (C).

**Supplementary Video 1.** Crystallization of dendrites. The video is presented at 2 $\times$  speed. The scale is  $8.738 \times 8.738 \mu\text{m}$ . Frames of the same event are presented in Figure 2.

**Supplementary Video 2.** Electron-beam-induced nucleation of dendrites. The time and scale are presented in the video. Frames of the same event are presented in Figure 3A–3C.

**Supplementary Video 3.** Electron-beam-induced crystal growth. The time and scale are presented in the video. Frames of the same event are presented in Figure 3D–3F.